Check for updates

Enhancement of acidic hydrogen evolution reaction efficiency through Cu/Ni-doped MFI-type protozeolite layered nanoclusters†

Xiaodi Zhang, Xiyuan Tong,‡ Junyang Wang,‡ Xinyu Zhu, Zhuozhe Li, Fang Fang, Kun Qian* and Yifeng E 🄳 *

We have prepared a highly active and stable copper-doped nickel electrocatalyst. Cu/Ni-doped MFI-type protozeolite layered nanoclusters electrodes have a large electrochemically active surface area (ECSA) and good HER activity, as well as excellent durability. The addition of Cu greatly increases hydrogen evolution reaction (HER) activity under acidic conditions. At the same time, the *in situ* grown $Cu_{2+1}O$ provides some activity, and in addition, the interface constructed between Cu and Ni further generates sufficient electrochemically active surface area. The activated Cu/Ni-doped MFI-type layered nanoclusters required only a 385 mV overpotential to generate 10 mA cm^{-2}, demonstrating efficient and stable activity with potential practical applications.

Introduction

The development of clean and sustainable energy sources is crucial for the future of our planet.[1] Hydrogen fuel, produced by water splitting through hydrogen evolution reaction (HER), is considered a key component of fuel cells.[2,3] However, the high activation energy required for water splitting presents a significant challenge for the development of efficient and cost-effective HER catalysts.[4,5] Noble metal catalysts, such as platinum and iridium, have been widely used due to their high activity and stability. However, their high cost and scarcity limit their practical application, especially for large-scale production.[6–8] To overcome the limitations posed by the high cost and scarcity of noble metals, researchers have been delving into the development of alternative catalysts. By exploring new materials and methods, they aim to find catalysts that are more affordable, sustainable, and effective for various applications.[9–11]

Common materials, especially transition metals, have been considered potential catalysts for HER due to their low cost and abundance.[12,13] Copper and nickel have emerged as promising alternatives for HER catalysis due to their excellent performance.[14,15] In addition, their doped materials have shown improved catalytic activity and stability.[16] The significance of replacing precious metals lies in the potential to reduce the cost and increase the scalability of HER catalysis, which is crucial for the development of renewable energy technologies.[17,18]

Materials doped with two metals, known as bimetallic catalysts, have shown improved catalytic activity and stability compared to their single-metal counterparts. This is due to the synergistic effect between the two metals, which can enhance the electronic and structural properties of the catalysts.[19] Bimetallic catalysts have been extensively studied for various applications, including HER catalysis.[20] The preparation methods for bimetallic catalysts involve using multiple precursors and synthesis techniques to control the composition, morphology, and surface properties of the catalysts.[21]

Protozeolites are amorphous particles that have short-range order and microporous characteristics. It can be extracted from growth solutions before crystallites emerge.[22] Protozeolite precursors with a zeolite embryo structure have better colloidal stability, adjustable silanol chemistry, and an easy crystallization feature compared to conventional starting amorphous gel particles. These features could benefit zeolite crystal growth through a nonclassical pathway.[23] As a common molecular sieve material, MFI-type zeolite is a type of crystalline aluminosilicate with a unique microporous structure. They are widely used in various fields due to their exceptional properties, such as high thermal stability, acidity, and selectivity.[24] The hydrothermal preparation method is commonly used to synthesize MFI-type zeolite materials, which involves using silicon and aluminum sources in the presence of a structure-directing agent and water. The resulting MFI-type zeolite materials possess a tetrahedral framework structure with uniform micropores, making them ideal for catalysis, adsorption, and separation.[25] MFI-type zeolite materials have been extensively studied in recent years for their potential applications in petrochemicals, fine chemicals, and environmental protection.[26,27] Zeolite itself has poor electrical conductivity, and its application in the field of

Jinzhou Medical University, Jinzhou, 121001, PR China. E-mail: eyf@jzmu.edu.cn; skyearth20032003@163.com

‡ Xiyuan Tong and Junyang Wang contributes equal to Xiaodi Zhang for this work.

electrocatalysis is limited, because their frame structure does not contain any redox metals,[28] but the introduction of metals into its frame structure shows excellent application prospects in the field of electrocatalysis. In this paper, protozeolite, which is usually an amorphous precursor of zeolite,[29,30] is used as a framework to introduce oxidized metals for the first time to explore its hydrogen evolution reaction performance as an electrocatalyst. The development of metal-doped MFI-type zeolite materials as efficient HER catalysts can contribute to the advancement of fuel cell technology and the promotion of sustainable energy systems.

In this work, we synthesized Cu/Ni-doped MFI-type protozeolite layered nanoclusters (Cu/Ni/MFI-PZ) with a large specific surface area. We also constructed Ni-substituted amorphous layered nanoclusters to improve the catalyst's hydrogen evolution activity and stability by embedding the oxidation state of Cu into the substrate. Furthermore, we explored the effect of electrochemical activation on the catalyst's hydrogen evolution performance, and it was found that electrochemical activation could enhance the hydrogen evolution effect of Cu/Ni/MFI-PZ.

Experimental

Reagents and materials

Anhydrous ethanol (99.7%), cupric sulfate ($CuSO_4 \cdot 5H_2O$, 99%, Tianjin Yongsheng Fine Chemical Co., Ltd.); tetraethyl orthosilicate (98%, tripropylamine (99%, Shanghai Aladdin Biochemical Technology Co., Ltd.); sodium aluminate ($NaAlO_2$, 41.0%, Liaoning Quanrui Reagent Co., Ltd.); nickelous chloride ($NiCl_2 \cdot 6H_2O$, 98%, Tianjin Guangfu Fine Chemical Research Institute); sulfuric acid (98%, Jinzhou Gucheng Chemical Reagent Co., Ltd.), all the reagents in our experiments was used without further purification. Deionized water was used throughout the experiment.

Synthesis of Cu/Ni/MFI-PZ *via* hydrothermal method

MFI-type protozeolite layered nanoclusters (MFI-PZ) were synthesized by static hydrothermal method, 2.08 g tetraethyl orthosilicate, 0.1 g $NaAlO_2$, and 0.47 g tripropylamine were added to 9 mL water, transferred to a steel autoclave reactor with Teflon inner after thoroughly stirring, and then heated in a 448 K for 43 h. After the reaction, the resulting mixture was centrifuged at 12000 rpm for 10 minutes to obtain precipitation. Then, the solid-state sample was washed by ultrasound with water three times and once with ethanol, repeated three times to wash off impurities, and dried in a vacuum drying oven at 50 °C for 3 h. The synthesis methods of Ni-doped MFI-type protozeolite layered nanoclusters (Ni/MFI-PZ), Cu-doped MFI-type protozeolite layered nanoclusters (Cu/MFI-PZ) and Cu/Ni-doped MFI-type protozeolite layered nanoclusters (Cu/Ni/MFI-PZ) were the same as those of MFI-PZ, except that 0.42 g $NiCl_2$, 0.42 g $CuSO_4$, 0.42 g $CuSO_4$ and $NiCl_2$ were added, respectively.

Characterization and instrumentations

The TDM-10 X-ray diffractometer (XRD) and the high-resolution XRD (Bruker D8 Advance Powder X-ray diffraction (XRD) diffractometer.) are used for crystallization and phase analysis of Cu/Ni-

doped layered nanoclusters. Transmission electron microscopy (TEM) (JEOL JEM-2100 F microscope) are used for morphological analysis of the Cu/Ni-doped layered nanoclusters. And an energy dispersive spectrometer (EDS) for elemental analysis (JEOL JEM-2100 F microscope). Elemental analysis is performed by X-ray photoelectron spectroscopy (XPS, ULTRA AXIS[DLD]). Electrochemical measurements are performed using a standard three-electrode system using the CHI660E electrochemical workstation (Shanghai Chenhua Instrument Co., Ltd.).

Electrochemical measurements

Electrochemical testing was performed using an improved three-electrode system with modified glassy carbon electrodes (GCE) and Pt electrodes for the working electrode, carbon rod for the counter electrode, and a saturated calomel electrode (SCE) for the reference electrode. Before the test, the glassy carbon electrode was polished to the mirror surface on the suede with 0.2 μm alumina slurry. It was then washed with distilled water and ethanol for later use. The catalysts were dispersed with ethanol (20 mg mL^{-1}) and ultrasonically mixed evenly before use. 20 μL of the catalyst was evenly applied to the surface of the glassy carbon electrode each time and dried at room temperature. The performance of different modified electrodes was compared.

All tests were performed at 0.5 M H_2SO_4 in an inverted electrolytic cell. The linear sweep voltammetry (LSV) was used for the HER performance test, with a scanning range of 0 V to −1.5 V and a sweep speed of 100 mV s^{-1}. The amperometric *i–t* curve method (A *i–t* C) was used to study the electrochemical activity and stability of the catalyst, and the reduction potential was −1 V. The electric double-layer capacitance method determined the electrochemically active surface area (ECSA) of the catalyst. The electric double-layer capacitance (C_{dl}) measurement was obtained by changing the scanning speed of cyclic voltammetry (CV) in the non-faradaic potential range. The formula for calculating C_{dl} is as follows:

$$i_c = \nu C_{dl} \tag{1}$$

$$ECSA = C_{dl}/C_s \tag{2}$$

where i_c is the current and ν is the CV scan rate, plotting i_c against ν forms a linear relationship, where the slope is taken as C_{dl}. The C_{dl} is converted to ECSA *via* a C_s, assuming that the C_s of the ideal smooth oxide surface is 60 μF cm^{-2}.[31]

The measured potential is converted to a reversible hydrogen electrode (RHE) potential:

$$E_{RHE} = E_{SCE} + 0.241 + 0.059 \, pH \tag{3}$$

Results and discussion

The electrochemistry characterization of the Cu/Ni/MFI-PZ

Fig. 1 presents the linear sweep voltammetry (LSV) curve of Cu/Ni/MFI-PZ tested for hydrogen evolution activity in 0.5 M H_2SO_4 using a three-electrode system in an inverted electrolytic cell.
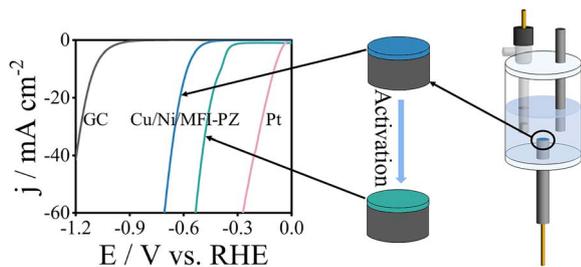
Fig. 1 LSV plot of modified electrode before and after activation in an inverted electrolytic cell.

The figure shows that the Cu/Ni/MFI-PZ overpotential at 10 mA cm^{-2} is approximately -580 mV, significantly lower than the blank GCE. Furthermore, the modified electrode was activated by the A i–t C method at a constant potential of -1 V for 4800 s, resulting in a decreased overpotential of -385 mV at 10 mA cm^{-2}. This direct electrochemical reduction activation lowered the overpotential by 195 mV. Compared to a platinum disk electrode under the same conditions, the overpotential was slightly higher by around 100 mV. These results demonstrate that the Cu/Ni/MFI-PZ exhibit excellent electrocatalytic activity for the hydrogen evolution reaction.

Characterization

As shown in Fig. 2A, the X-ray diffraction (XRD) pattern of the undoped layered nanoclusters exhibits a broad diffraction peak between 15° and 30°, according to previous experience, the broad diffraction peaks here are characteristic of the amorphous aluminosilicate phase.[32] To investigate the main factors affecting the hydrogen evolution performance of the catalyst, layered nanoclusters doped with Ni and Cu were designed, respectively. The Ni-doped layered nanoclusters have broad diffraction peaks at 15–30° and 30–40°, indicating that they still possess a disordered structure. As for the Cu-doped layered nanoclusters, in addition to the broad diffraction peak between 15° and 30°, new diffraction peaks emerge at approximately 29.6°, 36.4°, and 42.3°. These peaks correspond to the lattice planes of $Cu_{2+1}O$ (110), $Cu_{2+1}O$ (111) and $Cu_{2+1}O$ (200) (JCPDS card no. 05-0667), respectively. Indicating successful growth of $Cu_{2+1}O$ on the amorphous layered nanoclusters. In contrast, the XRD spectrum of the Cu/Ni/MFI-PZ only shows diffraction peak at 36.4° and 42.3° in addition to the broad diffraction peak between 15° and 30°, corresponding to the lattice planes of

$Cu_{2+1}O$ (111) and $Cu_{2+1}O$ (200) (JCPDS card no. 05-0667). The results show that after the introduction of Cu element into the system, the crystallinity of the (110), (111) and (200) crystal planes are weakened. Fig. 2B shows the high-resolution XRD patterns of the Cu/Ni/MFI-PZ before and after electroreduction. Compared to the Cu/Ni/MFI-PZ before electroreduction, the reduced Cu/Ni/MFI-PZ does not form new crystal structures. Instead, the original peaks become broader and less defined after reduction, suggesting enhanced disorder in the catalyst structure.

The HRTEM image (Fig. 3B) of the as-synthesized Cu/Ni/MFI-PZ revealed lattice fringes of 0.2139 nm and 0.2195 nm, corresponding to the d-spacing of (200) crystal plane of $Cu_{2+1}O$.

The lattice spacing of 0.2418 nm corresponds to the d-spacing of (111) crystal plane of $Cu_{2+1}O$, consistent with the XRD results, indicating partial embedding of Cu within the amorphous Ni/MFI-PZ. No lattice fringes were observed in the HRTEM image (Fig. 3D) of the electrochemically reduced Cu/Ni/MFI-PZ, suggesting the destruction of the $Cu_{2+1}O$ lattice by electroreduction and increased disorder of the nanoclusters. Energy dispersive X-ray spectroscopy (EDS) elemental mapping of the reduced Cu/Ni/MFI-PZ (Fig. 3F–H and S1†) showed uniform distribution of copper and nickel across the nanocluster surfaces. Fig. 3F shows the copper distribution, Fig. 3G shows the nickel distribution, Fig. 3H shows the overlay of the two elements, and Fig. S1† displays the elemental distribution within the framework. These results confirm the even dispersal of copper and nickel on the MFI-PZ.

The valence states of the Cu/Ni/MFI-PZ before and after the A i–t C process were further studied by X-ray photoelectron spectroscopy (XPS), and the results are shown in Fig. 4 and S2.† Fig. 4A and B are the high-resolution XPS spectra of the Cu/Ni/MFI-PZ. The high-resolution XPS spectra of Cu 2p in Fig. 4A show that the two peaks at 932.5 and 952.5 eV belong to the 2p$_{3/2}$ and 2p$_{1/2}$ spin–orbit splitting of Cu$^+$, confirming the existence of $Cu_{2+1}O$. The peaks at 934.8 and 954.7 eV are derived from 2p$_{3/2}$ and 2p$_{1/2}$ of Cu^{2+}, indicating the coexistence of Cu$^+$ and Cu^{2+}. The high-resolution XPS spectra of Ni 2p in Fig. 4B show that the peaks of 856.1 and 873.7 eV belong to the 2p$_{3/2}$ and 2p$_{1/2}$ characteristic peaks of Ni^{2+}, while the peaks of 857.7 and 875.4 eV belong to the 2p$_{3/2}$ and 2p$_{1/2}$ characteristic peaks of Ni^{3+}. The high-resolution XPS spectra of Cu 2p in Cu/Ni/MFI-PZ after A i–t C reduction are shown in Fig. 4C. The binding energy remains almost unchanged. The 2p$_{3/2}$ and 2p$_{1/2}$ characteristic peaks belonging to Cu$^+$ become stronger, while the 2p$_{3/2}$ and 2p$_{1/2}$ characteristic peaks belonging to Cu^{2+} become weaker, indicating the reduction of part of Cu^{2+} to Cu$^+$. Similar changes are observed in the high-resolution XPS spectra of Ni 2p in Fig. 4D. The 2p$_{3/2}$ and 2p$_{1/2}$ characteristic peaks belonging to Ni^{3+} weaken, while the 2p$_{3/2}$ and 2p$_{1/2}$ characteristic peaks belonging to Ni^{2+} become stronger. The high-resolution XPS spectra of other elements in Cu/Ni/MFI-PZ are shown in Fig. S2,† and their elements (Al, Si, C, O) show little change after electroreduction compared to the spectra before electroreduction. After the Cu/Ni/MFI-PZ are reduced by A i–t C, some metals are reduced to a lower valence state and deposited on the electrode. This results in the destruction of the crystal lattice of
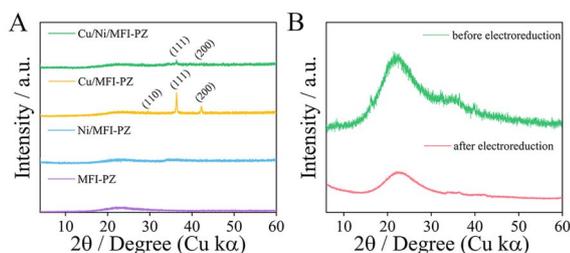

Fig. 2 (A) The XRD pattern of the as-synthesized different doping and without doping MFI-PZ, (B) the high-resolution XRD pattern of the Cu/Ni/MFI-PZ before and after electroreduction.
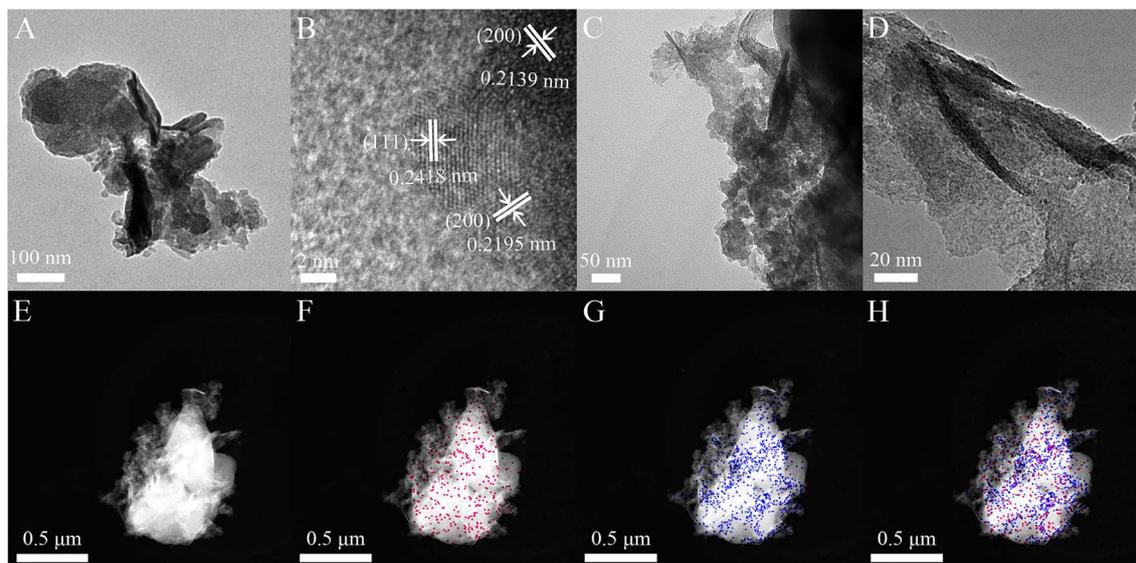
Paper

Fig. 3 Transmission electron microscopy (TEM) and high-resolution TEM (HRTEM) images of Cu/Ni/MFI-PZ. (A) TEM and (B) HRTEM images of the as-synthesized Cu/Ni/MFI-PZ. (C) TEM and (D) HRTEM images of the Cu/Ni/MFI-PZ after electrochemical reduction. Energy-dispersive X-ray spectroscopy (EDS) elemental mapping images of the electrochemically reduced Cu/Ni/MFI-PZ showing (E) overall morphology, (F) Cu distribution, (G) Ni distribution, and (H) overlay of Cu and Ni distributions.
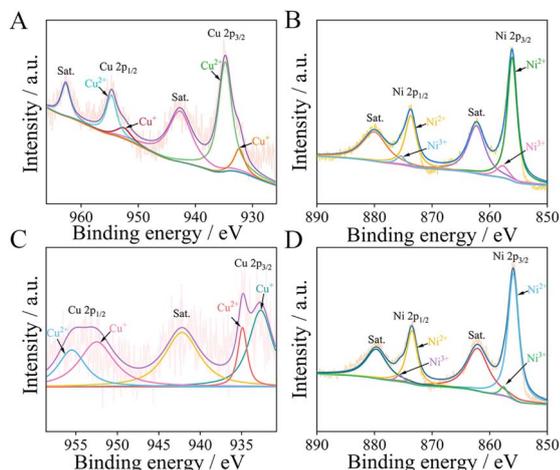

Fig. 4 The high-resolution XPS spectra of Cu 2p and Ni 2p before and after electroreduction. (A) The Cu 2p spectrum of the product before electroreduction. (B)The Ni 2p spectrum of the product before electroreduction. (C) The Cu 2p spectrum of the product after electroreduction. (D) The Ni 2p spectrum of the product after electroreduction.

$Cu_{2+1}O$, which increases the surface area of the catalyst. The destruction enhances the number of catalytic sites and improves the catalytic performance. This conclusion is also confirmed by the proportion of element distribution in EDS and XPS, where the Cu element exhibits the highest loss after electroreduction, as Table S1† shows.

Electrocatalytic performance of the Cu/Ni/MFI-PZ

The HER performance of Cu/Ni/MFI-PZ/GC electrodes were directly measured in 0.5 M H_2SO_4 solution, as Fig. 5 shows.

Fig. 5A shows the overpotential of Cu/Ni/MFI-PZ/GC is 580 mV (at 10 mA cm^{-2}), and its HER activity is better than that of a single metal, which indicates that the combination of Ni and Cu produced more active sites and increased the catalytic rate of H_2 generation. The effect of activation time on the hydrogen evolution performance of different modified electrodes was studied. Activation was carried out using the A i–t C method at a potential of −1 V, with the electrolyte being a 0.5 M H_2SO_4
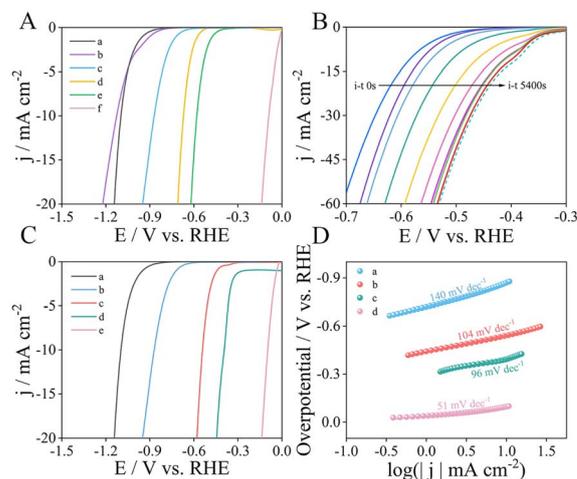

Fig. 5 (A) HER polarization curves (LSV) of Cu/Ni/MFI-PZ/GC (e), Cu/MFI-PZ/GC (d), Ni/MFI-PZ/GC (c), MFI-PZ/GC (b), GC (a) and Pt (f). (B) LSV curves of Cu/Ni/MFI-PZ/GC were measured after A i−t C electroreduction at −1 V in 0.5 M H_2SO_4 for the different activation times. (C) HER polarization curves for Cu/Ni/MFI-PZ/GC (d), Cu/MFI-PZ/GC (c), Ni/MFI-PZ/GC (b) after optimal activation time and comparison with Pt (e) and GC (a). (D) Tafel plot for Pt (d), Cu/Ni/MFI-PZ/GC (c), Cu/MFI-PZ/GC (b), Ni/MFI-PZ/GC (a).

solution. LSV curves were determined every 600 seconds to obtain LSV maps of Cu/Ni/MFI-PZ/GC, Ni/MFI-PZ/GC, and Cu/MFI-PZ/GC at different activation times. Fig. 5B shows that the hydrogen evolution performance of Cu/Ni/MFI-PZ/GC improves with the increased activation time. The LSV curve no longer changes once the activation time reaches 4800 s, indicating that 4800 s is the optimal activation time for Cu/Ni/MFI-PZ/GC. Similarly, Cu/MFI-PZ/GC exhibits an optimal activation time of 1800 s (Fig. S4A†), while Ni/MFI-PZ/GC loses its hydrogen evolution activity after activation (Fig. S4B†). Fig. S4C† shows the curves of the overpotential of Cu/Ni/MFI-PZ/GC (curve a), Cu/MFI-PZ/GC (curve b), and Ni/MFI-PZ/GC (curve c) at 10 mA cm^{-2} concerning activation time. The overpotential of Cu/Ni/MFI-PZ/GC and Cu/MFI-PZ/GC decreases with the increase in activation time, reaching -385 mV and -540 mV at their respective optimal activation times.

The HER performance of various modified electrodes at the optimal activation time was measured in 0.5 M H$_2$SO$_4$ solution. It is clear from Fig. 5C that the HER activity of Ni/MFI-PZ/GC is much lower than that of Cu/Ni/MFI-PZ/GC, indicating that Cu plays a crucial role in the HER process. Fig. 5D shows Tafel plots of different modified electrodes, except for Pt (51 mV dec^{-1}), the Tafel slope of Cu/Ni/MFI-PZ/GC (96 mV dec^{-1}) is higher than that of Cu/MFI-PZ/GC (104 mV dec^{-1}) and Ni/MFI-PZ/GC (140 mV dec^{-1}).

To compare the performance of various catalysts, we used the electrochemical surface area (ECSA) to normalize the current density (mA cm^{-2}).[33] This means that the current density is normalized to the geometric area of the electrode. The larger the ECSA, the higher the current density, indicating better performance of the catalyst.[34] The ECSA of all the electrodes was determined using the cyclic voltammetry (CV) curve method at different scanning rates, as shown in Fig. S3.† A linear relationship between the scanning rate and the charging current (i_c) was observed on the different electrodes. The slope of this relationship represents the double-layer capacitance (C_{dl}), as shown in Fig. S3F.† The ECSA for the GC, MFI-PZ/GC, Ni/MFI-PZ/GC, Cu/MFI-PZ/GC, and Cu/Ni/MFI-PZ/GC electrodes were measured to be 0.139 cm^2, 0.107 cm^2, 0.196 cm^2, 0.226 cm^2, and 0.736 cm^2, respectively. Among them, the ECSA of MFI-PZ/GC is smaller than that of GC. This is because as a precursor of zeolite, the original zeolite is mainly composed of some amorphous silicate, whose specific surface area is related to conductivity. Its structure does not contain redox metals and has low conductivity. Affected by the charge and discharge capacitance, the calculated C_{dl} is smaller,[35,36] resulting in its ECSA being lower than that of GC.

The results show that the ECSA of the catalyst is greatly increased after adding Cu. Previous studies have shown that the addition of copper to the metal catalyst coatings has been an effective method to increase the surface area and intrinsic catalytic activity of the material, which helps to generate a large number of active sites and enhance the HER activity.[37,38] In this study, the Cu/Ni/MFI-PZ exhibits good HER activity, not only due to the enhancement of the ECSA but also because the dissolution of Cu into Ni leads to the lattice distortion of Cu (Fig. 2A), resulting in a synergistic effect between Ni and Cu.
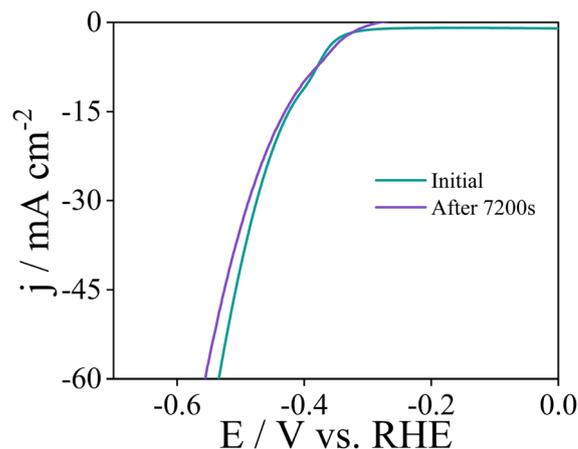

Fig. 6 Comparison of LSV curves at the initial and after stability tests for HER stability of Cu/Ni/MFI-PZ/GC.

Furthermore, the XPS results show that the activation process increases the amount of Cu$^+$ in the composite material (Fig. 4A and C), which enhances the charge transfer capability of the catalyst. The presence of Cu$^+$ in the catalyst not only serves as the active center for the reaction but also promotes electron transfer.[39,40]

HER stability of Cu/Ni/MFI-PZ/GC

To evaluate the stability of different modified electrodes in acidic media, an A i–t C reduction of 7200 s at a potential of -1 V was performed, as shown in Fig. 6. The current density remained consistent with the initial curve after the stability test, indicating the excellent catalytic stability of Cu/Ni/MFI-PZ and its practical applicability. Ni/MFI-PZ was catalytically deactivated after long-term cathodic reduction (Fig. S4D†), while Cu/MFI-PZ showed no deactivation after the 7200 s stability test (Fig. S4E†). During the long-term reaction, the stability of the Ni component could not be well maintained, which may have been due to the dissolution of Ni in the acidic electrolyte. However, during the activation process, Cu^{2+} was reduced to Cu$^+$. The presence of Cu$^+$ not only serves as the active center of the reaction but also promotes electron transfer, making up for the loss caused by the dissolution of the component in the electrolyte and maintaining the stability of the composite material. This suggests that Cu$_{2+1}$O has good electrocatalytic hydrogen evolution activity and stability and significantly improves hydrogen evolution performance in Cu/MFI-PZ. Therefore, Cu/Ni/MFI-PZ also exhibits good stability.

Conclusions

In this study, we synthesized Ni-doped MFI-type protozeolite layered nanoclusters to improve the hydrogen evolution performance. Cu$^+$ and Cu^{2+} were subsequently introduced on this basis to form Cu/Ni-doped MFI-type protozeolite layered nanoclusters, and the results showed that the double-doped layered nanoclusters exhibited better hydrogen evolution performance. Cu$_{2+1}$O significantly enhanced the hydrogen

evolution performance of Ni-doped MFI-type protozeolite layered nanoclusters and played a crucial role in improving the catalysts' stability. Additionally, the activation process is an important strategy to regulate the oxidation state of Cu catalysts to affect the hydrogen evolution performance of catalysts significantly. This result will provide a reference for improving the hydrogen evolution performance of amorphous catalysts.

Data availability

All relevant data are within the manuscript and its additional files.

Author contributions

Xiaodi Zhang: experiment, data curation, wrote the original draft. Yifeng E: conceptualization, supervision, wrote – reviewing, and funding acquisition. Xinyu Zhu: visualization and investigation. Xiyuan Tong: validation, wrote – review and editing. Kun Qian: methodology, wrote – review and funding acquisition. Zhuozhe Li: theoretical calculation. Fang Fang: software.

Conflicts of interest

The authors declare that they have no known competing financial interests or personal relationships that could have appeared to influence the work reported in this paper.

Acknowledgements

Notes and references

1 A. Razmjoo, L. G. Kaigutha, M. V. Rad, M. Marzband, A. Davarpanah and M. Denai, *Renewable Energy*, 2021, **164**, 46–57.

2 P. Ahmadi and A. Khoshnevisan, *Int. J. Hydrogen Energy*, 2022, **47**, 26758–26769.

3 P. M. Bodhankar, P. B. Sarawade, P. Kumar, A. Vinu, A. P. Kulkarni, C. D. Lokhande and D. S. Dhawale, *Small*, 2022, **18**, 2107572.

4 X. Ning and G. Lu, *Nanoscale*, 2020, **12**, 1213–1223.

5 Y. Yu, J. Zhou and Z. Sun, *Adv. Funct. Mater.*, 2020, **30**, 2000570.

6 M.-L. Cui, Y.-S. Chen, Q.-F. Xie, D.-P. Yang and M.-Y. Han, *Coord. Chem. Rev.*, 2019, **387**, 450–462.

7 P. L. Cabot, M. V. Martínez-Huerta and F. Alcaide, *Johnson Matthey Technol. Rev.*, 2023, **67**, 249–265.

8 C. Huang, P. Qin, Y. Luo, Q. Ruan, L. Liu, Y. Wu, Q. Li, Y. Xu, R. Liu and P. K. Chu, *Mater. Today Energy*, 2022, **23**, 100911.

9 X. Xu, L. Pan, Q. Han, C. Wang, P. Ding, J. Pan, J. Hu, H. Zeng and Y. Zhou, *J. Catal.*, 2019, **374**, 237–245.

10 Z. Zhuang, J. Huang, Y. Li, L. Zhou and L. Mai, *ChemElectroChem*, 2019, **6**, 3570–3589.

11 L. Lin, P. Sherrell, Y. Liu, W. Lei, S. Zhang, H. Zhang, G. G. Wallace and J. Chen, *Adv. Energy Mater.*, 2020, **10**, 1903870.

12 H. Sun, Z. Yan, F. Liu, W. Xu, F. Cheng and J. Chen, *Adv. Mater.*, 2020, **32**, 1806326.

13 A. Parra-Puerto, K. L. Ng, K. Fahy, A. E. Goode, M. P. Ryan and A. Kucernak, *ACS Catal.*, 2019, **9**, 11515–11529.

14 K. S. Bhat and H. Nagaraja, *ChemistrySelect*, 2020, **5**, 2455–2464.

15 U. Y. Qazi, R. Javaid, N. Tahir, A. Jamil and A. Afzal, *Int. J. Hydrogen Energy*, 2020, **45**, 33396–33406.

16 H. Yuan, S. Zheng, S. Sang, J. Yang, J. Sun, Z. Ma and X. Wang, *Int. J. Hydrogen Energy*, 2022, **47**, 11827–11840.

17 L. Yan, B. Zhang, J. Zhu, Y. Li, P. Tsiakaras and P. K. Shen, *Appl. Catal., B*, 2020, **265**, 118555.

18 Q. Wu, J. Wang, X. Wang, L. Wang, J. Wei, R. Xu and L. Yang, *Fuel*, 2024, **357**, 129994.

19 I. V. Yentekakis, P. Panagiotopoulou and G. Artemakis, *Appl. Catal., B*, 2021, **296**, 120210.

20 C. H. Lee, S. Pahari, N. Sitapure, M. A. Barteau and J. S.-I. Kwon, *ACS Catal.*, 2022, **12**, 15609–15617.

21 C. Wei, Y. Sun, G. n. G. Scherer, A. C. Fisher, M. Sherburne, J. W. Ager and Z. J. Xu, *J. Am. Chem. Soc.*, 2020, **142**, 7765–7775.

22 Q. Zhang, J. Li, X. Wang, G. He, L. Li, J. Xu, D. Mei, O. Terasaki and J. Yu, *J. Am. Chem. Soc.*, 2023, **145**, 21231–21241.

23 Y. Liu, X. Wang, J. Li, Q. Zhang, Z. Niu, S. Wang, Y. Gao, M. Gao, R. Bai, Y. Zhou, W. Fan, O. Terasaki, J. Xu and J. Yu, *Angew. Chem., Int. Ed.*, 2023, **62**, e202312131.

24 W. Xia, Y. Huang, C. Ma, S. Li, X. Wang, K. Chen and D. Liu, *Fuel*, 2023, **341**, 127675.

25 L. Wang and Z. Bian, *Chemosphere*, 2020, **239**, 124815.

26 A. Palizdar and S. M. Sadrameli, *Fuel*, 2020, **264**, 116813.

27 Y. Liu, L. He, L. Wang, D. Ma, L. Ma, Q. Yao and M. Sun, *Fuel*, 2024, **359**, 130442.

28 R. Srivastava, *Catal. Today*, 2018, **309**, 172–188.

29 Q. Zhang, A. Mayoral, O. Terasaki, Q. Zhang, B. Ma, C. Zhao, G. Yang and J. Yu, *J. Am. Chem. Soc.*, 2019, **141**, 3772–3776.

30 Q. Zhang, G. Chen, Y. Wang, M. Chen, G. Guo, J. Shi, J. Luo and J. Yu, *Chem. Mater.*, 2018, **30**, 2750–2758.

31 B. Chi, H. Lin, J. Li, N. Wang and J. Yang, *Int. J. Hydrogen Energy*, 2006, **31**, 1210–1214.

32 K. Onik, M. Gackowski, M. A. Derewinski and B. Sulikowski, *J. Phys. Chem. C*, 2018, **122**, 25983–25991.

33 D. Voiry, M. Chhowalla, Y. Gogotsi, N. A. Kotov, Y. Li, R. M. Penner, R. E. Schaak and P. S. Weiss, *ACS Nano*, 2018, **12**, 9635–9638.

34 C. Wei, S. Sun, D. Mandler, X. Wang, S. Z. Qiao and Z. J. Xu, *Chem. Soc. Rev.*, 2019, **48**, 2518–2534.

35 C. C. L. McCrory, S. Jung, J. C. Peters and T. F. Jaramillo, *J. Am. Chem. Soc.*, 2013, **135**, 16977–16987.

36 S. Jung, C. C. L. McCrory, I. M. Ferrer, J. C. Peters and T. F. Jaramillo, *J. Mater. Chem. A*, 2016, **4**, 3068–3076.

37 Q. Sun, Y. Dong, Z. Wang, S. Yin and C. Zhao, *Small*, 2018, **14**, 1704137.

38 H. L. S. Santos, P. G. Corradini, M. Medina and L. H. Mascaro, *Int. J. Hydrogen Energy*, 2020, **45**, 33586–33597.

39 L. Li and Z. Zhang, *Chem. Eng. J.*, 2022, **434**, 134811.

40 Z. Zhang, R. Chen, L. Wang, X. Chen, J. Ding, J. Zhang, H. Wan and G. Guan, *Appl. Surf. Sci.*, 2023, **609**, 155297.